PAPER

Porous FTO thin layers created with a facile one-step Sn^{4+}-based anodic deposition process and their potential applications in ion sensing†

Kuan-Ting Lee and Shih-Yuan Lu*

Porous fluorine-doped tin oxide (FTO) thin layers were created from commercial FTO glass with a novel, facile, one-step Sn^{4+}-based anodic deposition process. The Sn^{2+} necessary for the anodic deposition of SnO_2 was generated *in situ* from the starting Sn^{4+} such that a comparable competition between deposition and acid-etching of SnO_2 became possible, leading to a rich morphological evolution of the deposit. The fluoride ions released from the acid-etching of the starting FTO layer were later incorporated into the newly deposited SnO_2 to make it fluorine-doped, resulting in the formation of a conductive, porous FTO layer. This unique FTO product may find a wide range of applications in processes requiring large surface areas for the accommodation of active sites to host functional interfacial events and excellent electric conductivities for charge transfer/transport involved in the interfacial events. To demonstrate its applicability, this conductive porous FTO thin layer was applied to the sensing of nitrate ions, which play a fundamental role in a wide range of environmental and biological processes. A simple device was developed for the sensing of nitrate ions based on surface charge-modulated adsorption of nitrate ions and measurements of consequent currents. At 0.5 M HNO_3, the porous FTO showed a 55 fold sensitivity improvement over the commercial FTO. In buffer solutions of a specific pH value, the cation effects on ion sensitivities were also discussed. A low detection limit of 10^{-8} M was achieved for nitrate ion sensing with the present porous FTO layer.

Introduction

Tin oxide is a well-studied n-type semiconductor with a direct bandgap of 3.6 eV[1] and has been intensively investigated for a wide range of applications, including sensors,[2,3] anode materials for energy conversion and storage,[4–6] and catalysts.[7,8] For a successful application of tin oxide in the above mentioned areas, large surface areas for the accommodation of active sites to host functional interfacial events, such as adsorption, redox reactions, and catalytic chemical reactions, are essential. This structural characteristic can be achieved with porous and nanoscale featured structures. Consequently, a great deal of research effort has been placed on the development of a wide range of nanostructured tin oxide, including nanoparticles,[9,10] thin films,[11,12] nanorods,[13,14] nanowires,[15,16] and nanograss,[17] with a wide variety of methods such as hydrothermal processes,[17,18] chemical vapor depositions (CVD),[19] electrochemical depositions,[11,20–22] anodization,[23,24] and sol–gel processes.[25,26] Among them, electrochemical deposition is advantageous in several process and product aspects. It is simple and cost-effective, often operated at low temperatures, scalable for large-scale production, versatile in

terms of product composition and morphology, and capable of creating films on complex surfaces. Furthermore, it creates the targeted functional nanomaterials and nanostructures directly on conductive substrates with excellent adhesions, an advantage particularly critical for charge transfer/transport involved applications.

For charge transfer/transport involved applications, it is highly desirable to enhance the electric conductivity of the tin oxide nanostructure so that the necessary charge transfer/transport processes can be more easily carried out to improve the device performances. Enhancements in electric conductivity of tin oxide can be readily achieved *via* fluorine doping, the so-called fluorine-doped tin oxide (FTO). FTO, because of its excellent visible light transparency and electric conductivity, has found extensive applications in optoelectronics, display, and photovoltaic devices as a transparent conductive electrode.[27,28] FTO films are commonly fabricated *via* gas phase processes, chemical or physical, including CVD,[19] spray pyrolysis,[29,30] thermal evaporation,[3,31] pulsed laser evaporation,[32–34] and magnetron sputtering,[35] with magnetron sputtering currently viewed as the most popular industrial production method. The preparation of FTO nanostructures with electrochemical means however received very little, if not no, research attention.

The many different electrochemical methods for tin oxide (instead of FTO) preparation reported in the literature may be classified into two main categories: cathodic and anodic

Department of Chemical Engineering, National Tsing Hua University, Hsinchu, Taiwan. E-mail: SYLu@mx.nthu.edu.tw
† Electronic supplementary information (ESI) available. See DOI: 10.1039/c2jm33060a

deposition. Normally, SnO$_2$ deposits are created at anodes through oxidation of tin sources. With the anodic deposition processes, Sn^{2+} or Sn^0 sources are supplied to be oxidized at the anodes to form SnO$_2$ (of an oxidation state of IV for Sn). As for depositions occurring at cathodes, a rare practice, Sn^{4+} sources were first hydrolyzed by hydroxyl ions produced *in situ* at the cathode from aqueous nitrate salts, followed by a condensation reaction of the hydroxides to form SnO$_2$.[36] In this article, uniquely, we developed a novel, facile, one-step Sn^{4+}-based anodic deposition process to create thin conductive porous fluorine-doped tin oxide layers from commercial FTO glass and demonstrated their excellent potential in nitrate ion sensing. To our best knowledge, this is the first example of Sn^{4+}-based anodic deposition of SnO$_2$. The Sn^{2+} ions necessary for oxidation formation of SnO$_2$ at the anode were supplied *in situ* through reduction of the starting Sn^{4+} ions. This indirect supply of Sn^{2+} ions was essential to enable a comparable competition between deposition and acid-etching of SnO$_2$ for the creation of the conductive porous SnO$_2$ layer. The fluoride ions released from the acid-etching of the FTO substrate served as a fluoride source for the newly deposited SnO$_2$ to make it fluorine-doped. As an end result, the present process was able to create conductive porous FTO layers from commercial FTO glass. Note that FTO glass is a commercial product, making the present electrochemical treatment process well-suited for future commercialization.

The potential applications of this unique product of conductive porous FTO layers were demonstrated by examining its performance in nitrate ion sensing. Nitrate ions play a fundamental role in a wide range of environmental and biological processes,[37] and several methods have been developed for the measurement of nitrate ion concentrations, including ultraviolet ray/visible light, fluorescence/spectrophotometric methods,[38–40] liquid phase chromatographic analyses,[41] biosensors,[42] and electrochemical methods.[43] Here, we develop a simple device for the sensing of nitrate ions based on surface charge-modulated adsorption of nitrate ions and measurements of consequent currents. At 0.5 M HNO$_3$, the porous FTO showed a 55 fold sensitivity improvement over the commercial FTO. In buffer solutions of a specific pH value, the cation effects on ion sensitivities were also discussed. Based on a criterion of three standard deviations from the baseline, it was found that a low detection limit of 10^{-8} M was achieved with the present porous FTO layer.

Experimental methods

The electrochemical treatment of commercial FTO glass (6–8 Ω □$^{-1}$, 2 mm × 20 mm × 20 mm) was conducted in an electrolyte composed of an aqueous solution of 0.07 M SnCl$_4$·5H$_2$O (Baker, 99%) and 0.3 M oxalic acid, with a Pt wire (0.5 mm × 50 mm) and the FTO glass serving as the cathode and anode, respectively. The set up was operated at 7 V at room temperature. The cathode and anode were kept 25 mm apart and the electrolyte was stirred at ambient conditions. After the electrochemical treatment, the electrodes were rinsed with DI water and dried in air for later use.

The crystalline structure of the samples was determined by an X-ray diffractometer (XRD, MAC Science, MXP18, Cu Kα), and the surface elemental composition and oxidation state were characterized by an X-ray photoelectron spectroscope (XPS, VG

ESCA Scientific Theta Probe). The sheet resistances were measured with the standard four-probe method using a four-point probe meter (Zentech 502BC). Raman spectra were recorded with a high resolution confocal Raman microscope (HOROBA, Lab Ramhr) at room temperature. The morphologies of the samples were observed by using a field emission scanning electron microscope (FESEM, Hitachi, S-4700) at an accelerating voltage of 15 kV and an atomic force microscope (AFM, Park Systems, XE-70). The transmission spectra were obtained with a UV-visible spectrometer (Hitachi, U-2800).

A facile current-based sensing system of nitrate ions was developed in this article. The sample was immersed into a solution containing nitrate ions at room temperature and the resulting currents were recorded by a source meter (Keithley 236) at a preset potential of 1 V. DI water was taken as the comparison base for the calculation of sensitivity, S, defined as $S = (I_N - I_W)/I_W$. Here, I_N is the current recorded for the nitrate solution and I_W for the DI water.

Results and discussions

A thin, porous layer was created at the top of the FTO glass after the electrochemical treatment. The electrochemical treatment was conducted in oxalic acid at 7 V for 30 min with SnCl$_4$·5H$_2$O serving as the Sn ion source. Fig. 1(A) shows a top view SEM
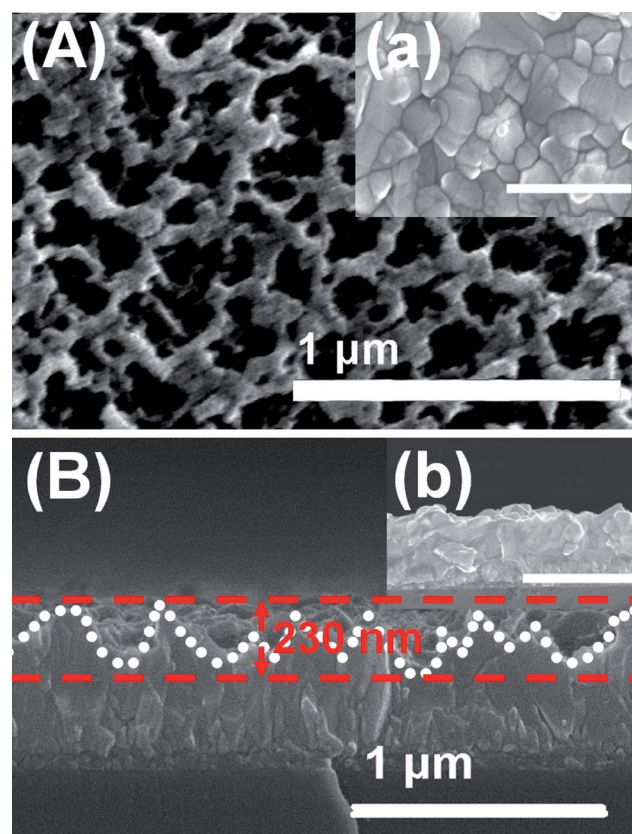

Fig. 1 (A) Top and (B) cross-sectional view SEM images of the electrochemically treated FTO samples (7 V, oxalic acid, 30 min), with corresponding SEM images for the untreated FTO samples as insets for comparison. Dotted lines were used to outline the pores in (B) as an eye-guide. The scale bars of the two inset images are 1 μm.
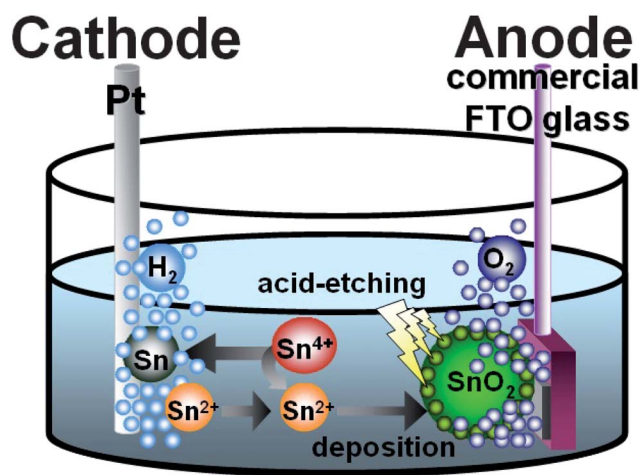
Fig. 2 Schematic for the electrochemical treatment cell.

image of the product with a top view SEM image of the starting, untreated FTO shown in the inset for comparison. Evidently, the original dense structure of the untreated FTO became porous after the electrochemical treatment. The pore size ranged from around 60 to 250 nm. Fig. 1(B) shows the corresponding cross-sectional SEM images for the treated and untreated (shown in the inset) samples. One can readily identify a distinct rougher top layer of around 230 nm thick from the image of the treated sample. Pores with widths of several tens to a couple of hundred nanometers can be outlined from the images, in good agreement with the corresponding top view image. Because of the pore formation, the surface roughness of the FTO layer increased from 10 to 36 nm as was determined with an AFM. It is to be stressed here that the roughness of 36 nm for the porous product may be underestimated because of the depth resolution limit of the AFM tip.

The formation of the porous layer is a competition result between deposition and etching of SnO_2. As illustrated in Fig. 2, there are three main events occurring during the electrochemical treatment, including *in situ* supply of Sn^{2+} from Sn^{4+}, anodic deposition of Sn^{2+} at the anode to form SnO_2, and acidic etching of SnO_2 to create pores. The use of Sn^{4+} instead of Sn^{2+} as the starting precursor is the key to the success of the present process for pore formation. The gradual supply of Sn^{2+} from Sn^{4+} enables a comparable competition between deposition and etching of SnO_2. If Sn^{2+} is used as the starting precursor, the deposition rate will outperform the etching rate, leading to unwanted morphology. Once the supply of Sn^{2+} is under control, the morphological characteristics of the porous layer can be modulated through adjustment in treatment time, type of acids used, and applied potential.

To further understand the mechanism of pore formation, we investigated the variations of solution pH, layer morphology, layer thickness, and cell current with respect to the treatment time. Fig. 3(A) shows the cell current *versus* treatment time plot, with layer thickness and morphology embedded at several time marks for discussion. The cell current dropped sharply at the beginning and leveled off to a relatively stable value. Initially, the reacting species at the proximity of the electrode surface were abundant and their consumption generated high cell currents through relevant redox reactions. The supply rate of these reacting species from the bulk of the electrolyte through mass

convection and diffusion however lagged behind the consumption rate, leading to a drop in redox reaction rates and thus the cell currents. The mass transfer rate soon matched the consumption rate and a dynamic equilibrium was thus established to maintain a constant cell current level.

Interestingly, the FTO layer thickness as estimated from the cross-sectional SEM images first rapidly increased (from 652 to 960 nm in 5 min) and then gradually decreased to values not much higher than the starting thickness (706 nm at the 15 min mark and 681 nm at the 30 min mark), and increased again slightly (697 nm at the 60 min mark). This phenomenon implies that the whole electrochemical treatment involves an initial rapid growth followed by a moderate dissolution, and finally a slow regrowth stage. It can be manifested by the competition between electrochemical deposition and etching. A much faster deposition gives the initial rapid growth; an etching dominant period leads to the moderate dissolution; a slight edge of deposition results in the final slow re-growth. More interestingly, the layer morphology showed matching characteristics with the corresponding variations in layer thickness. At the fast growth stage,
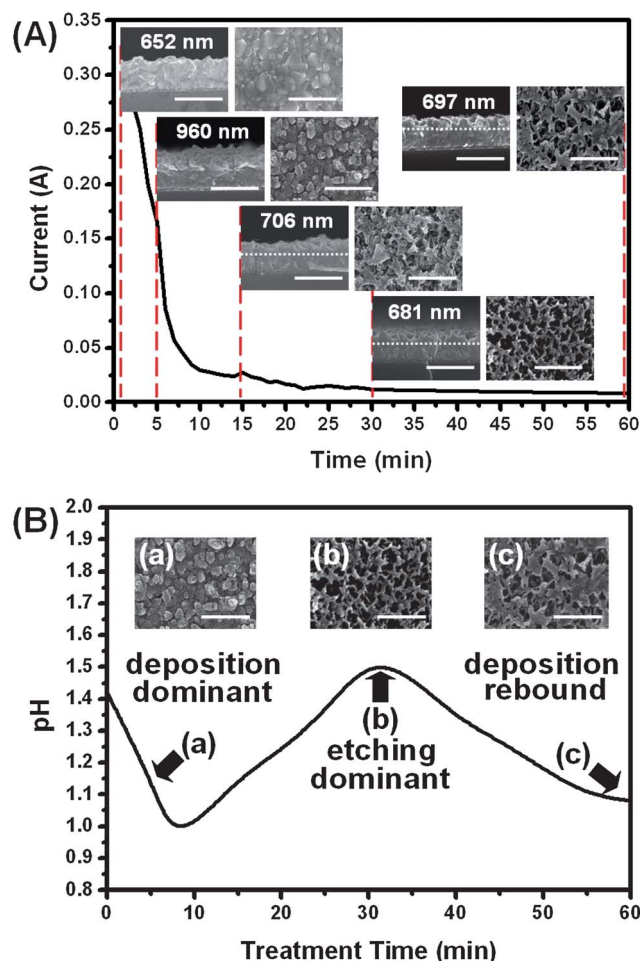

Fig. 3 (A) The cell current and (B) solution pH *versus* treatment time curves for the oxalic acid system operated at 7 V. The top and cross-sectional view SEM images of the treated FTO layer at several characteristic time marks were shown for discussion. The corresponding thicknesses of the FTO layers were also included for discussion. The scale bars are all 1 μm in length.

the growing layer remained non-porous, although the surface became rougher from the non-uniform growth of the growing fronts of SnO_2. And no distinct rougher top layer can be identified from the corresponding cross-sectional SEM image. For the two samples collected at the moderate dissolution stage, the ones collected at the 15 and 30 min marks, they appeared porous from the top view and distinct rougher layers were evident from the cross-sectional view as highlighted with dashed lines. The porousness of the 15-min sample was less well-developed than that of the 30-min sample, with some regions remaining yet to be etched. At the slow re-growth stage, some pores were filled from the re-deposition as is evident from the top view image of the 60-min sample.

The solution pH evolution is presented in Fig. 3(B). Three distinct characteristic regions can be identified from the plot. The solution pH first decreased to a minimum in about 8 min, then increased to a maximum at the 31 min mark, and went on a decreasing trend till the end of the treatment. The time spans of the three regions matched quite well with those of the three morphological regions identified from Fig. 3(A). Here, we placed the top view SEM images of the three samples collected from the 5-min, 30-min, and 60-min marks to go with the pH evolution plot to stress the close match between them. From Fig. 3(A) and (B), one can conclude that the whole electrochemical treatment can be divided into three stages: deposition-dominant, followed by etching-dominant, and finally deposition rebound.

Accordingly, we proposed the following reaction mechanisms. Before the electrochemical treatment started, Sn^{4+} was reduced by $H_2C_2O_4$ to generate Sn^{2+} which was the ion source for the formation of SnO_2 at the anode.[44]

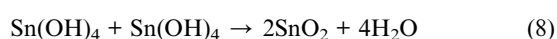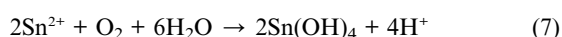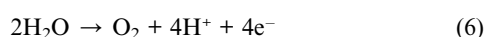$$Sn^{4+} + C_2O_4^{2-} \rightarrow Sn^{2+} + 2CO_2 \tag{1}$$
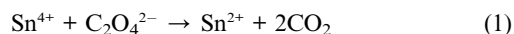
The generation of CO_2 bubbles was experimentally observed before the application of an electric potential to the treatment cell. Once the electrochemical treatment started, more Sn^{2+} was produced through a partial reduction of Sn^{4+} at the cathode (Reaction (2)).[36] Part of the Sn^{2+} thus produced was further reduced to form Sn on the cathode surface (Reaction (3)),[36] and part of it got transported to the anode to be oxidized there to form SnO_2. Certainly, Sn^{4+} was also reduced to Sn at the cathode surface (Reaction (4)).[1] In addition, H_2 bubbles were generated at the cathode from the reduction of H^+ (Reaction (5)).[45]
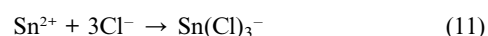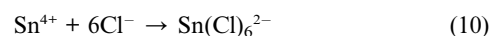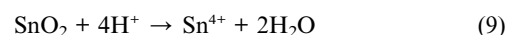
Cathode:

$$Sn^{4+} + 2e^- \rightarrow Sn^{2+} \tag{2}$$

$$Sn^{2+} + 2e^- \rightarrow Sn \tag{3}$$

$$Sn^{4+} + 4e^- \rightarrow Sn \tag{4}$$

$$2H^+ + 2e^- \rightarrow H_2 \tag{5}$$

Anode:

$$2H_2O \rightarrow O_2 + 4H^+ + 4e^- \tag{6}$$

$$2Sn^{2+} + O_2 + 6H_2O \rightarrow 2Sn(OH)_4 + 4H^+ \tag{7}$$

$$Sn(OH)_4 + Sn(OH)_4 \rightarrow 2SnO_2 + 4H_2O \tag{8}$$

At the anode, H_2O was first oxidized to form O_2 and H^+ (Reaction (6)).[21] The production of H^+ decreased the solution pH as observed from the initial drop in solution pH shown in Fig. 3(B). The production of O_2 bubbles was also experimentally observed. The Sn^{2+} generated at the pre-treatment stage and supplied through mass transfer from the partial reduction of Sn^{4+} at the cathode was oxidized to first form $Sn(OH)_4$ (Reaction (7)), that further went through a condensation reaction to form SnO_2 on the anode (FTO) surface (Reaction (8)).[11,21] The H^+ produced from Reaction (7) also helped to lower the solution pH. Reactions (7) and (8) led to the deposition of SnO_2 at the anode.

Besides Reactions (6)–(8), the following reactions may also occur simultaneously.

$$SnO_2 + 4H^+ \rightarrow Sn^{4+} + 2H_2O \tag{9}$$

$$Sn^{4+} + 6Cl^- \rightarrow Sn(Cl)_6^{2-} \tag{10}$$

$$Sn^{2+} + 3Cl^- \rightarrow Sn(Cl)_3^- \tag{11}$$

$$2Cl^- \rightarrow Cl_2 + 2e^- \tag{12}$$

Here, the formed SnO_2 was etched with H^+ (Reaction (9))[46] and the resulting Sn^{4+} formed $Sn(Cl)_6^{2-}$ with chloride ions,[46] thus enhancing further dissolution of SnO_2 through Reaction (9). The Sn^{4+} produced from Reaction (9) also got reduced by $C_2O_4^{2-}$ to form Sn^{2+} (Reaction (1)) that further formed $Sn(Cl)_3^-$ with chloride ions (Reaction (11)),[47] again indirectly enhancing Reaction (9). The chloride ions may also be oxidized to generate Cl_2 (Reaction (12)).[48] Reactions (9)–(11) together with Reaction (1) represent the etching process occurring at the anode, with Reaction (10) and Reactions (1) and (11) serving as the two enhancing routes for the etching.

The competition of the deposition and etching processes led to the characteristic evolutions in solution pH and product morphology as presented in Fig. 3(A) and (B). At the beginning of the electrochemical treatment, the deposition process was dominant, resulting in a decrease in solution pH (increase in H^+ concentrations) and growth of the non-porous SnO_2 layer. Once Sn^{2+} was consumed to reach some low concentration level, the deposition process was no longer dominant and the etching process took control with the favorable high H^+ concentrations. It is important to note that the presence of Cl^- is critical to the continuing dominance of the etching process since Reaction (9) was enhanced by chloride ions directly with the removal of Sn^{4+} through Reaction (10) and indirectly *via* Reactions (1) and (11). Since H^+ was consumed in the etching process, the solution pH increased with the treatment time during the etching-dominant stage. The deposit thickness decreased because of the etching, and porous structure evolved since the etching was disturbed by the gas bubbles produced from Reactions (6) and (12), leading to non-uniform etching for pore formation.

It is to be stressed that the deposition and etching processes occurred simultaneously, but that one was dominant over the other under different solution conditions. The etching reaction also attacked the fluorine-doped SnO_2 layer of the starting FTO glass and released fluoride ions. These fluoride ions can be incorporated into the newly deposited SnO_2 layer, making it fluorine-doped. The product porous layer was thus a porous

FTO layer, possessing good electric conductivities as discussed in a later section.

Once the chloride ions were consumed to reach some low concentration level, Reaction (9) ceased its domination since its enhancing reactions involving chloride ions became unfavorable. Under this condition, the deposition process re-gained its control and deposition prevailed again, only at a lower rate as judged from the less steep solution pH decreasing trend shown in Fig. 3(B). The deposition now took place in a porous medium and thus encountered greater mass transfer resistances to access the inner space of the porous medium. As a result, slower deposition rates were observed.

The effects of electrolytes were investigated by replacing oxalic acid with acetic acid. The results for the product morphology and solution pH evolutions are presented in Fig. 4(A) and (B). First, one notes the slower deposition growth, a thickness increase from 652 to 848 nm in 15 min, which is significantly less than that of the oxalic system, with an increase from 652 to 960 nm in 5 min. This phenomenon can be attributed to the lower supply rate of Sn^{2+} in the acetic acid system. For the oxalic acid system,
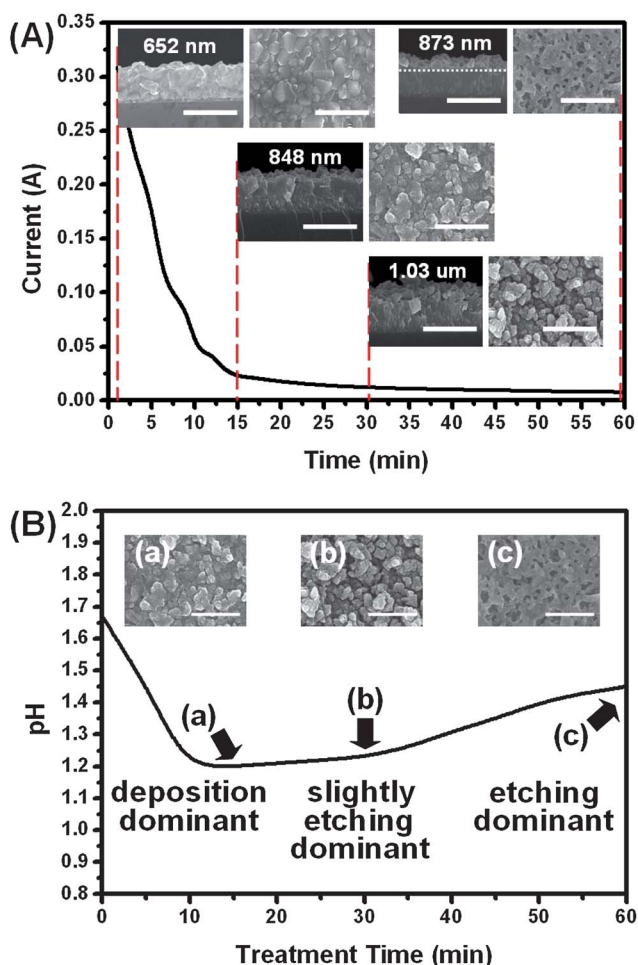

Fig. 4 (A) The cell current and (B) solution pH *versus* treatment time curves for the acetic acid system operated at 7 V. The top and cross-sectional view SEM images of the treated FTO layer at several characteristic time marks were shown for discussion. The corresponding thicknesses of the FTO layers were also included for discussion. The scale bars are all 1 μm in length.

Sn^{2+} was produced through Reaction (1) even before the electrochemical treatment started. As for the acetic acid system, acetate ions are not a reducing agent as are oxalate ions to reduce Sn^{4+} for the supply of Sn^{2+}. Experimentally, there were no bubbles observed after mixing the $SnCl_4$ solution with acetic acid. Furthermore, the transport of Sn^{2+} from the cathode to the anode *via* mass convection and diffusion was a relatively slower process. Consequently, the SnO_2 deposition through Reactions (7) and (8) was much slower than that in the oxalic acid system.

The solution pH reached a minimum at the time mark of 15 min, and slowly increased up to the time mark of 30 min. Opposite to the phenomena observed in the oxalic acid system, here the layer thickness kept increasing to 1.03 μm without evident pore formation at the time mark of 30 min. Several factors can be put together to explain these phenomena. First, recall that there were two enhancing routes for the etching reaction. One of them, the indirect one, was inactive in the acetic acid system since acetate ions cannot remove Sn^{4+} with Reaction (9) by reducing it to Sn^{2+}. This resulted in a slow etching and thus slow pickup in solution pH. Second, the etching rate was only slightly higher than the deposition rate. As a result, the deposition continued to increase the layer thickness, while the etching only partially consumed the deposits, not enough to create pores but only to roughen the deposit surface. If one examines closely the cross-sectional and top view images of the product layer obtained at the time mark of 30 min in Fig. 4(A), the significantly rougher surface can be clearly observed.

The increase in the solution pH speeded up at the time mark of 30 min, indicating a more dominating etching process. This phenomenon can be understood considering the depletion of Sn^{2+} for SnO_2 deposition. As a result of this etching dominance, a porous product layer, although not well developed, was obtained with a decreased layer thickness of 873 nm at the time mark of 60 min.

In addition to the treatment time and electrolyte, the applied potential is also an important treatment parameter. Four different applied potentials, 5, 6, 7, and 8 V, were used for the electrochemical treatment and the products obtained with a treatment time of 30 min in the oxalic acid system were characterized with UV-visible transmission spectra together with the corresponding top view SEM images to show their porousness. The results are shown in Fig. 5(A). Also included in Fig. 5(A) for comparison are the relevant data for untreated FTO glass. The pore size ranged from several tens of nanometers to a couple of hundred nanometers, with which the light passing through was significantly scattered, leading to reduced transmissions. For the untreated FTO glass, the transmission was maintained above 70%, with a sharp drop occurring at wavelengths below 350 nm, which was caused by the band to band absorption of SnO_2. With a bandgap of 3.6 eV, SnO_2 showed on-set absorptions at around 350 nm.

Evidently, with an applied potential of 5 V, the transmission spectrum remained unchanged, as did the top view morphology, as compared with the untreated ones. In fact, the layer thickness remained the same as that of the untreated sample. An applied potential of 5 V was enough to drive the usual electrolysis of water for H_2 and O_2 production at the cathode and anode, respectively, but not enough to trigger the oxidation–condensation reactions for SnO_2 formation under the present formulation.
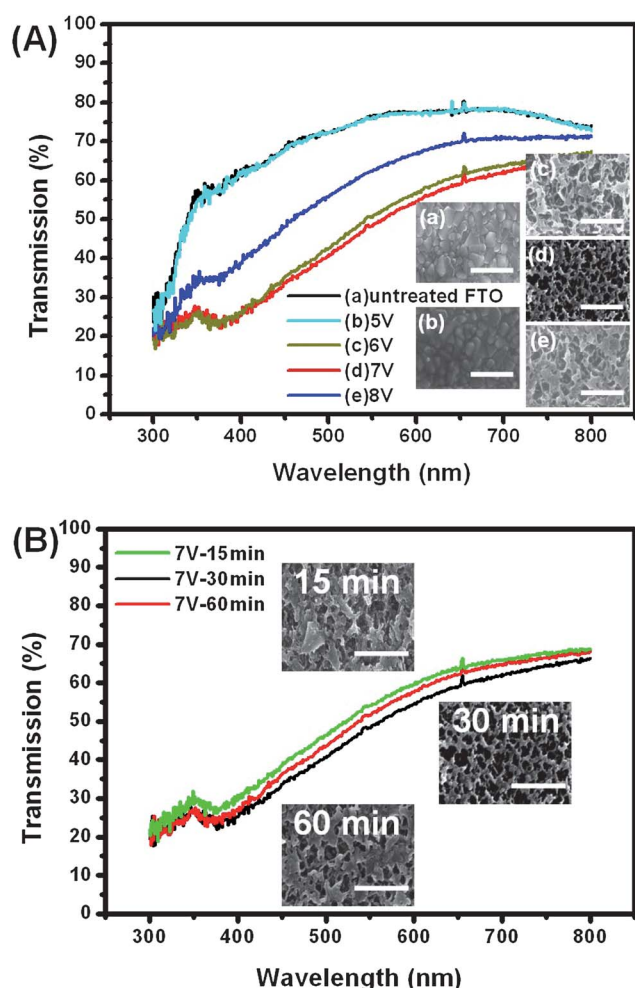
Fig. 5 (A) Transmission spectra of FTO samples, untreated and treated at 5, 6, 7, and 8 V in oxalic acid for 30 min. (B) Transmission spectra of FTO samples, treated at 7 V in oxalic acid for 15, 30, and 60 min. Corresponding top view SEM images were also included for discussion.

developed porous structures than that of the case of 30 min, and thus showed correspondingly higher transmission spectra. As discussed previously, the morphology of the product layer went through a pore development process followed by a pore blockage process. The 15-min sample was collected during the pore development stage, whereas the 60-min sample was collected during the pore blockage stage. And the 30-min sample was collected probably right at the transition point of the pore development to pore blockage stage, exhibiting the most well-developed porous structure and thus the lowest transmission spectra.

As mentioned earlier, the product layer in fact was FTO in chemical composition. The fluoride ions released from the etching of the starting FTO layer were incorporated into the later deposited SnO_2, making it fluorine-doped. This is critical for applications requiring not only porous structure for high functioning surface areas, but also low electric resistances for efficient charge transfer/transport. The surface elemental composition of the porous product layer was determined with XPS. The fluorine content did drop from 4.37 at.% for the untreated FTO sample to 1.48 at.% for the sample produced at 7 V for a treatment time of 30 min in the oxalic acid system. Here, we used XPS for the F content estimation to make sure that the result came from the product porous layer instead of being influenced by the starting FTO layer beneath it. For a sensing depth limit of less than 10 nm for XPS, the porous layer of around 30 nm can well shield the starting FTO layer from being sampled by the XPS measurement.

The existence of the less-F-doped SnO_2 porous layer will increase the sheet resistance of the sample. Table 1 summarizes the sheet resistance data for the untreated FTO sample and samples produced from applied potentials of 5, 6, 7, and 8 V with a treatment time of 30 min in the oxalic acid system. The 5 V-sample experienced no treatment effects as discussed earlier, and showed an almost identical sheet resistance value with that of the untreated FTO sample. This is in good agreement with the morphological observation and transmission spectrum data presented in Fig. 5(A). As for the porous layer containing samples, the sheet resistances increased slightly from 7.2 to 15–19 $\Omega\ \square^{-1}$, still low for many applications involving charge transfer/transport.

Fig. 6 displays the XRD patterns of the FTO glass before and after the electrochemical treatment. Both patterns matched very well with that of SnO_2 of the tetragonal phase (JCPDS 77-0447). No extra diffraction peaks can be identified from both patterns, indicating that SnO_2 was the sole appreciable crystalline product at the anode after the treatment. If one examines the (110) diffraction peaks closely as enlarged in the inset, there can be observed left-shifts in 2θ of the F-doped samples from that of the SnO_2. The left-shift in 2θ was caused by the F-doping, and was more pronounced for the untreated FTO sample because of its higher doping concentration,[49–51] in good agreement with the XPS data. Here, substitution of one O^{2-} by two F^- is necessary to maintain electroneutrality, and thus results in an increase in

Increasing the applied potential to 6 V was enough to drive the deposition and etching of SnO_2, and a partially developed pore structure was obtained after a 30 min treatment. Note that higher applied potentials offer greater driving forces for the relevant electrochemical and subsequent chemical reactions to proceed to initiate the deposition and etching of SnO_2. As compared with the product of well-developed pore structure from the case of 7 V, that from the case of 6 V appeared to be partially developed, whereas that from the case of 8 V showed the partial blockage of pores from the re-deposition of SnO_2 occurring at the third stage of the electrochemical treatment. The transmission spectra showed the matching trend with the porousness development, with the product from the case of 7 V giving the lowest transmission spectrum.

The effects of treatment time on the porousness of the product layer were also investigated and the results are shown in Fig. 5(B). Here, the samples were prepared with an applied potential of 7 V in the oxalic acid system. We compared samples collected at treatment times of 15, 30, and 60 min. The corresponding top view SEM images were also included for comparison. Evidently, the products from the cases of 15 and 60 min both possessed less

Table 1 The sheet resistance of porous FTO films

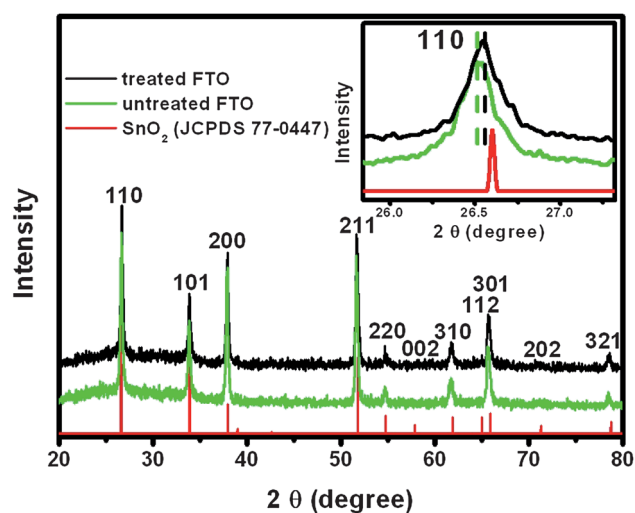|	Untreated FTO	5 V	6 V	7 V	8 V
$\Omega\ \square^{-1}$	7.2 ± 0.8	7.5 ± 0.5	15.2 ± 1.1	17.1 ± 0.9	19.1 ± 1.3

Fig. 6 XRD pattern of FTO samples untreated and treated at 7 V in oxalic acid for 30 min. Inset is a local enlargement of the (110) diffraction peak.

lattice parameters, giving left-shifts in 2θ.[49,51] Fig. S1† shows the XRD pattern of the cathode after the treatment. Expectedly, the product obtained at the cathode was Sn (JCPDS 89-4898) from the reduction of Sn^{4+} and Sn^{2+}. Fig. S2† shows the XPS of the treated FTO sample, which displays an evident spin-orbit doublet at 486.7 ($3d_{5/2}$) and 495.1 eV ($3d_{3/2}$) for the confirmation of the oxidation state of Sn^{4+} for the porous product layer.[22,52–54] Fig. S3† shows the Raman spectrum for the FTO glass before and after the electrochemical treatment. There can be identified three Raman shifts located at around 571, 633, and 774 cm^{-1}, with the latter two contributed by crystalline SnO_2 and the first one arising from the size effect of the nanosized SnO_2 grains.[55] The grain sizes of the untreated and treated FTO glass can be estimated with the Scherrer equation based on the broadening of the (110) diffraction peak of Fig. 6 to be around 40 nm, supporting the size effect.

The present product has demonstrated its excellent potential as a sensing host for nitrate ions. Here, we devised a simple sensing device for nitrate ions. As illustrated in Fig. 7, the electrochemically treated FTO glass was immersed into a nitrate containing solution, for example nitric acid. At a preset potential, the resulting current was recorded. The value of the current was a function of the nitrate ion concentration as discussed below. Depending on the solution pH, the surface of the fluorine-doped SnO_2 may be positively or negatively charged or remain neutral. When the solution pH is lower than the point of zero charge (PZC) of SnO_2, around 4.3, the surface hydroxide ligands of SnO_2 will be predominantly protonated to form $-OH_2^+$, giving an overall positive charge for the SnO_2 surface.[56–58] On the contrary, if the solution pH is higher than the PZC, the surface hydroxide ligands of SnO_2 will be predominantly deprotonated to form $-O^-$, giving an overall negative charge for the SnO_2 surface.[58,59] Protonated hydroxide ligand, $-OH_2^+$, attracts NO_3^- to the SnO_2 surface, leading to a higher electron density there. Note that, disregarding the solution pH, the three types of hydroxide ligands, positively charged $-OH_2^+$, neutral $-OH$, and negatively charged $-O^-$, are all present on the surface of the

SnO_2, only the relative amounts vary with the solution pH. When the solution pH is lower than PZC, $-OH_2^+$ outnumbers $-O^-$, giving an overall positive charge for the SnO_2 surface, and the opposite is true for the case of pH higher than PZC. Consequently, positively charged SnO_2 surfaces attract more NO_3^- to the SnO_2 surface and thus receive higher electron density lifts, leading to larger currents. With this mechanism, the concentration of the nitrate ion translates into the current value recorded, and higher nitrate concentrations give larger currents.

Fig. 8(A) shows the sensitivity *versus* HNO_3 concentration plot for four different types of sensing hosts, including FTO treated in oxalic acid for 30 min, FTO treated in acetic acid for 30 min and 60 min, and untreated FTO, representing four distinct morphologies of the sensing host, corresponding to well-developed porous, roughened but nonporous, partially porous, and flat nonporous structures, respectively. Evidently, the sensitivity gets leveled off at both ends of the concentration range. This is expected since the comparison base for the definition of the sensitivity is taken as the DI water environment. At low HNO_3 concentrations, the environment is close to DI water and thus results in limited differences in recorded currents. At high HNO_3 concentrations, the extent of attachment of NO_3^- to the SnO_2 surface becomes saturated and the current increase at increasing HNO_3 concentration diminishes. Also evident from the plot is that the sensitivity becomes more pronounced with an increase in the extent of porousness of the sensing host. The more porous structure possesses higher surface areas to host more sensing events, and thus higher sensitivities. In fact, the untreated FTO sample showed almost no sensing ability as compared with the treated ones. As a comparison, at 0.5 M HNO_3, the treated FTO sample of a well-developed porous structure showed a 55 fold sensitivity improvement over the untreated FTO sample. Furthermore, with the best treated FTO sample, there were still appreciable sensitivities detectable at HNO_3 concentrations down to 10^{-9} M.

The reproducibility of the HNO_3 sensing was demonstrated in Fig. 8(B). The FTO sample treated in oxalic acid for 30 min was taken for this demonstration. The analyte solution was changed from DI water to 10^{-3} M HNO_3, then to 1 M HNO_3, and this
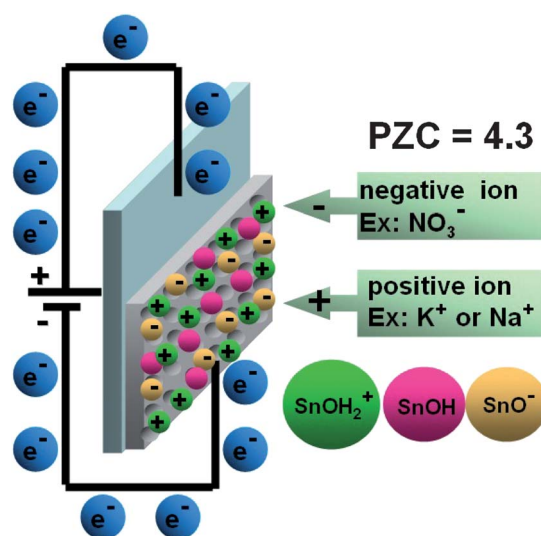

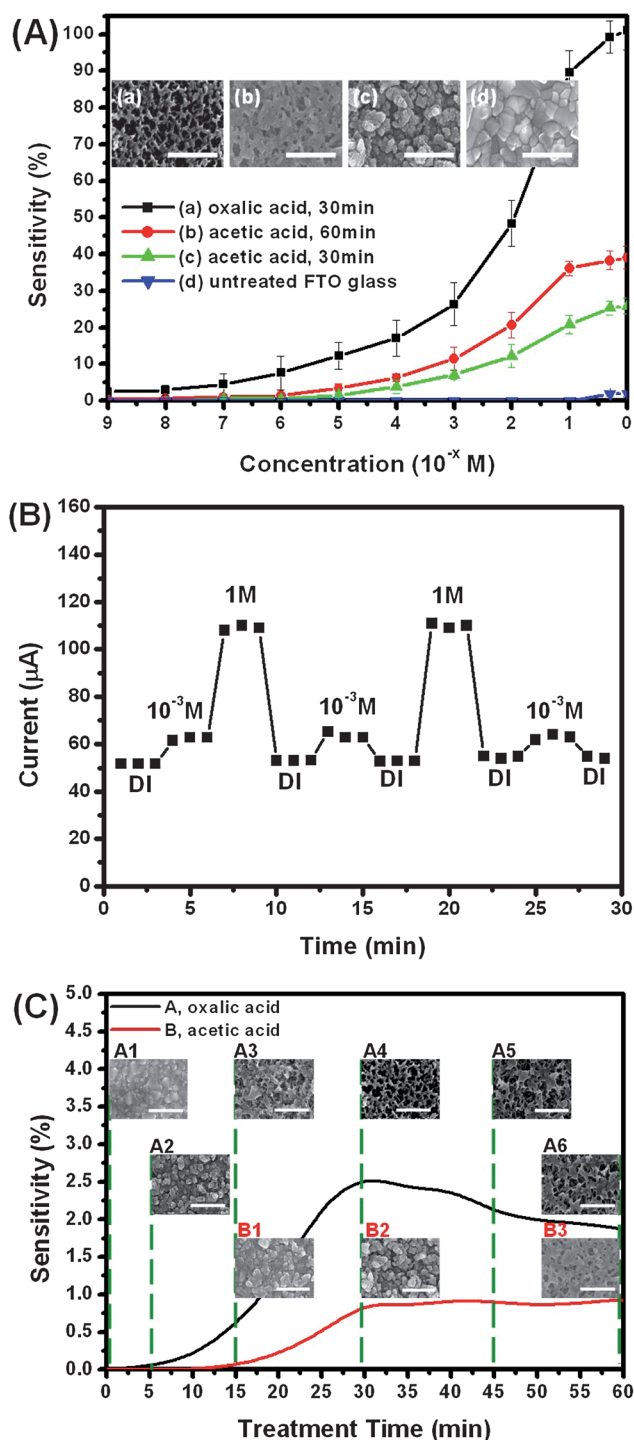**Fig. 7** Illustration of the simple device for current measurements.

Fig. 8 (A) Sensitivity *versus* HNO$_3$ concentration plot for FTO samples untreated and treated at 7 V in oxalic acid for 30 min and in acetic acid for 30 and 60 min. (B) Current *versus* time plot for FTO sample treated at 7 V in oxalic acid for 30 min. (C) Sensitivity *versus* treatment time for FTO samples treated at 7 V in oxalic acid and acetic acid.

cycle was repeated to check the reproducibility. The current level increased with increasing HNO$_3$ concentration as expected, and reproduced well for the same sensing conditions.

The effects of treatment time and electrolyte for the preparation of the sensing host were also investigated and the results are presented in Fig. 8(C). Also included for discussion purposes

were the corresponding top view SEM images. The comparison was made for the case of HNO$_3$ concentration of 10^{-9} M. It can be concluded that the sensitivity basically goes with the porousness of the sensing host. The use of oxalic acid in the electrolyte created much more well-developed porous layers than those created by using acetic acid, and thus the corresponding products possessed higher sensitivities. A treatment time of 30 min for the oxalic acid system gave the most well-developed porous structure and thus the highest sensitivity.

To investigate the cation effects of the analyte, we used a buffer solution of a desired pH to set the surface charge state of the SnO$_2$, and measured the resulting currents for two different analytes, NaNO$_3$ and KNO$_3$. Two scenarios were studied, pH3 (<PZC) for positively charged and pH5 (>PZC) for negatively charged SnO$_2$. Fig. 9(A) shows the current *versus* contact time plots for six different solutions, including buffer solutions of pH3 and pH5, and NaNO$_3$ and KNO$_3$ solutions in the two different buffers. Interestingly, for positively charged SnO$_2$, the currents obtained from both analytes were higher than those from the buffer solution, and the opposite trend was true for the
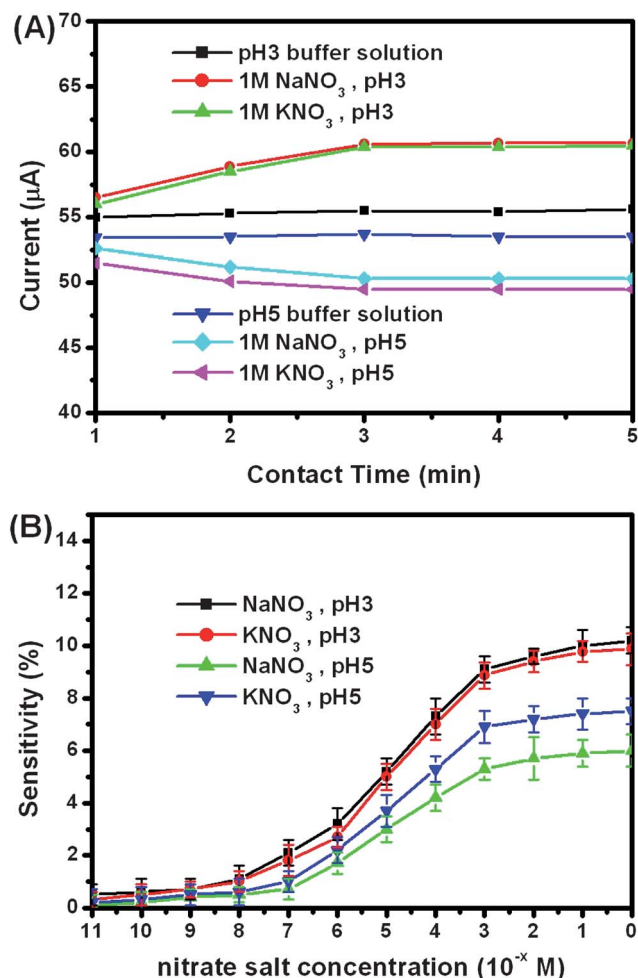

Fig. 9 (A) Current *versus* contact time for FTO samples immersed in buffer solutions of pH3 and pH5, and NaNO$_3$ and KNO$_3$ solutions in buffers pH3 and pH5. (B) Sensitivity *versus* nitrate salt concentration for FTO samples immersed in NaNO$_3$ and KNO$_3$ solutions of buffers pH3 and pH5. The FTO samples were treated at 7 V in oxalic acid for 30 min.

16266 | *J. Mater. Chem.*, 2012, **22**, 16259–16268

This journal is © The Royal Society of Chemistry 2012

negatively charged SnO$_2$. Furthermore, the currents collected for NaNO$_3$ were higher than those for KNO$_3$, and the current differences between the two analytes were significantly larger for the pH5 case. These phenomena can be understood as the following. For positively charged SnO$_2$, the dominant current-determining species was NO$_3^-$, which was attracted to the positively charged SnO$_2$ surface to increase the electron density there to give larger currents. Here, the cation played a minor role and thus the kind of cation did not have much affect on the resulting currents. When the SnO$_2$ was negatively charged, cations become the dominant species for determining the currents. They are attracted to the SnO$_2$ surface to decrease the electron density there to produce smaller currents. Since cations are now a dominant species, their characteristics affect the resulting currents to a significant extent. Note that the cations exist in an aqueous environment as hydrated ions. The ionic size of the hydrated Na$^+$ (0.79 nm) is in fact larger than that of the hydrated K$^+$ (0.53 nm),[60] and thus the hydrated Na$^+$ ion exerts less electron drawing force on the charged SnO$_2$ surface than does the hydrated K$^+$ ion, thereby leading to larger currents. It is worth noting that the effect of cations on the resulting currents depends on the electron drawing ability of the cations, regardless of their valences. In addition, the plot also reveals the fast kinetics of the ion adsorption process, from which stable currents were reached within 3 min of the contact time.

Fig. 9(B) shows the sensitivity *versus* nitrate salt concentration plot for four analyte solutions, including NaNO$_3$ and KNO$_3$ in the two buffer solutions, respectively. The sensitivity here was defined as $|I_A - I_B|/I_B \times 100\%$. Here, I_A and I_B are the currents detected for the analyte and corresponding buffer solutions, respectively. It is evident that the sensitivity gets leveled off at both ends of the concentration range. This is expected since the comparison base for the definition of the sensitivity is taken as the buffer solution. At low analyte concentrations, the environment is close to a pure buffer solution and thus limited differences in recorded currents results. At high analyte concentrations, the extent of ion adsorptions of both anions and cations to the SnO$_2$ surface becomes saturated and the current deviations from those of the corresponding buffer solution at increasing analyte concentration diminish. For positively charged SnO$_2$ surfaces (the pH3 case), the cations played a minor role in determining the currents, and thus the sensitivity curves were quite close to each other, insensitive to the kind of cation species. On the contrary, for negatively charged SnO$_2$ surfaces (the pH5 case), the cations became the dominant species for the determination of the current values, showing significant variations in sensitivity between the two analytes. The sensitivities achieved by KNO$_3$ were higher than those of NaNO$_3$ because of the smaller currents obtained for the case, resulting from the stronger electron drawing ability of the hydrated K$^+$. For the sensing of NaNO$_3$ at pH3, a low detection limit of 10^{-8} M was achieved based on a criterion of three standard deviations from the baseline, demonstrating the excellent potential of the present conductive, porous FTO layer in ion sensing.

Conclusions

A novel, facile, one-step Sn^{4+}-based anodic deposition process was developed, by which conductive, porous FTO layers were created from commercial FTO glass. The unique design of the indirect and *in situ* supply of Sn^{2+} from the starting Sn^{4+} *via* partial reductions for the anodic deposition of SnO$_2$ is critical for the successful creation of the porous structure. The potential applications in ion sensing of this unique product of conductive, porous FTO layers were demonstrated by investigating the surface-adsorption effected current variation behavior modulated by the pH-dependent surface charge characteristics of SnO$_2$. Because of the high surface areas offered by the porous structure, the present product exhibited an excellent ion sensing potential, far exceeding that of commercial FTO glass, and achieved a low detection limit of 10^{-8} M for NaNO$_3$ at pH3.

Notes and references

1 D. Chu, Y. Masuda, T. Ohji and K. Kato, *Chem. Eng. J.*, 2011, **168**, 955–958.
2 S. K. Mahadeva and J. Kim, *Sens. Actuators, B*, 2011, **157**, 177–182.
3 N. V. Hieu, L. T. N. Loan, N. D. Khoang, N. T. Minh, D. T. Viet, D. C. Minh, T. Trung and N. D. Chien, *Curr. Appl. Phys.*, 2010, **10**, 636–641.
4 M. Xu, M. Zhao, F. Wang, W. Guan, S. Yang and X. Song, *Mater. Lett.*, 2010, **64**, 921–923.
5 Y. F. Wang, J. W. Li, Y. F. Hou, X. Y. Yu, C. Y. Su and D. B. Kuang, *Chem.–Eur. J.*, 2010, **16**, 8620–8625.
6 R. S. Mane, J. Chang, D. Ham, B. N. Pawar, T. Ganesh, B. W. Cho, J. K. Lee and S. H. Han, *Curr. Appl. Phys.*, 2009, **9**, 87–91.
7 S. Wang, J. Huang, Y. Zhao, S. Wang, X. Wang, T. Zhang, S. Wu, S. Zhang and W. Huang, *J. Mol. Catal. A: Chem.*, 2006, **259**, 245–252.
8 Q. R. Zhao, *Trans. Nonferrous Met. Soc. China*, 2009, **19**, 1227–1231.
9 J. Liu, Y. Lu, J. Liu, X. Yang and X. Yu, *J. Alloys Compd.*, 2010, **496**, 261–264.
10 S. Z. Kang, Y. Yang and J. Mu, *Colloids Surf., A*, 2007, **298**, 280–283.
11 J. J. M. Vequizo, J. Wang and M. Ichimura, *Jpn. J. Appl. Phys.*, 2010, **49**, 125502–125505.
12 W. Hamd, Y. C. Wu, A. Boulle, E. Thune and R. Guinebretière, *Thin Solid Films*, 2009, **518**, 1–5.
13 D. Lei, M. Zhang, Q. Hao, L. Chen, Q. Li, E. Zhang and T. Wang, *Mater. Lett.*, 2011, **65**, 1154–1156.
14 X. Wang, W. Liu, H. Yang, X. Li, N. Li, R. Shi, H. Zhao and J. Yu, *Acta Mater.*, 2011, **59**, 1291–1299.
15 L. V. Thong, L. T. N. Loan and N. V. Hieu, *Sens. Actuators, B*, 2010, **150**, 112–119.
16 H. C. Wu, Y. C. Huang, I. K. Ding, C. C. Chen, Y. H. Yang, C. C. Tsai, C. D. Chen and Y. T. Chen, *Adv. Funct. Mater.*, 2011, **21**, 474–479.
17 Y. Wang, M. Guo, M. Zhang and X. Wang, *Thin Solid Films*, 2010, **518**, 5098–5103.
18 Y. L. Wang, M. Guo, M. Zhang and X. D. Wang, *CrystEngComm*, 2010, **12**, 4024–4027.
19 Y. C. Lee, O. K. Tan, H. Huang, M. S. Tse and H. W. Lau, *IEEE Trans. Nanotechnol.*, 2007, **6**, 465–468.
20 K. H. Wu and S. Y. Lu, *Electrochem. Solid-State Lett.*, 2005, **8**, D9–D11.
21 S. L. Chou, J. Z. Wang, H. K. Liu and S. X. Dou, *Electrochem. Commun.*, 2009, **11**, 242–246.
22 S. T. Chang, I. C. Leu and M. H. Hon, *J. Alloys Compd.*, 2005, **403**, 335–340.
23 J. H. Jeun, H. S. Ryu and S. H. Hong, *J. Electrochem. Soc.*, 2009, **156**, J263–J266.
24 H. C. Shin, J. Dong and M. Liu, *Adv. Mater.*, 2004, **16**, 237–240.
25 Z. Li, W. Shen, Z. Wang, X. Xiang, X. Zu, Q. Wei and L. Wang, *J. Sol-Gel Sci. Technol.*, 2009, **49**, 196–201.
26 J. Zhang and L. Gao, *J. Solid State Chem.*, 2004, **177**, 1425–1430.
27 S. M. Kong, Y. Xiao, K. H. Kim, W. I. Lee and C. W. Chung, *Thin Solid Films*, 2011, **519**, 3173–3176.
28 Z. Yang, T. Xu, S. Gao, U. Welp and W. K. Kwok, *J. Phys. Chem. C*, 2010, **114**, 19151–19156.
29 C. C. Lin, M. C. Chiang and Y. W. Chen, *Thin Solid Films*, 2009, **518**, 1241–1244.

This journal is © The Royal Society of Chemistry 2012

J. Mater. Chem., 2012, **22**, 16259–16268 | 16267

30 A. A. Yadav, E. U. Masumdar, A. V. Moholkar, K. Y. Rajpure and C. H. Bhosale, *Phys. B*, 2009, **404**, 1874–1877.

31 S. Shukla, V. Venkatachalapathy and S. Seal, *J. Phys. Chem. B*, 2006, **110**, 11210–11216.

32 R. D. Vispute, V. P. Godbole, S. M. Chaudhari, S. M. Kanetkar and S. B. Ogale, *J. Mater. Res.*, 1988, **3**, 1180–1186.

33 C. K. Kim, S. M. Choi, I. H. Noh, J. H. Lee, C. Hong, H. B. Chae, G. E. Jang and H. D. Park, *Sens. Actuators, B*, 2001, **77**, 463–467.

34 T. C. Avenue and K. Tong, *Appl. Phys. A: Mater. Sci. Process.*, 2005, **81**, 959–962.

35 H. Ahn, J. H. Noh, S. B. Kim, R. A. Overfelt, Y. S. Yoon and D. J. Kim, *Mater. Chem. Phys.*, 2010, **124**, 563–568.

36 X. Chen, J. Liang, Z. Zhou, H. Duan, B. Li and Q. Yang, *Mater. Res. Bull.*, 2010, **45**, 2006–2011.

37 W. S. Jobgen, S. C. Jobgen, H. Li, C. J. Meininger and G. Wu, *J. Chromatogr., B: Anal. Technol. Biomed. Life Sci.*, 2007, **851**, 71–82.

38 D. Tsikas, *J. Chromatogr., B: Anal. Technol. Biomed. Life Sci.*, 2007, **851**, 51–70.

39 M. M. Tarpey, D. A. Wink and M. B. Grisham, *Am. J. Physiol.*, 2004, **286**, R431–R444.

40 M. Grau, U. B. H. Cotta, P. Brouzos, C. Drexhage, T. Rassaf, T. Lauer, A. Dejam, M. Kelm and P. Kleinbongard, *J. Chromatogr., B: Anal. Technol. Biomed. Life Sci.*, 2007, **851**, 106–123.

41 S. B. Butt, M. Riaz and M. Z. Iqbal, *Talanta*, 2001, **55**, 789–797.

42 Z. Dai, H. Bai, M. Hong, Y. Zhu, J. Bao and J. Shen, *Biosens. Bioelectron.*, 2008, **23**, 1869–1873.

43 F. Bedioui and N. Villeneuve, *Electroanalysis*, 2003, **15**, 5–18.

44 R. N. Sahoo, P. K. Naik and S. C. Das, *Hydrometallurgy*, 2001, **62**, 157–163.

45 J. R. Parga, V. Vazquez, G. Gonzalez and M. M. Cisneros, *Chem. Eng. Technol.*, 2010, **33**, 1582–1590.

46 D. M. Sherman, K. V. Ragnarsdottir, E. H. Oelkers and C. R. Collins, *Chem. Geol.*, 2000, **167**, 169–176.

47 B. N. Stirrup and N. A. Hampson, *Surf. Technol.*, 1977, **5**, 429–462.

48 A. Kraft, *Platinum Met. Rev.*, 2008, **52**, 177–185.

49 S. Wu, S. Yuan, L. Shi, Y. Zhao and J. Fang, *J. Colloid Interface Sci.*, 2010, **346**, 12–16.

50 R. Shi, G. Huang, J. Lin and Y. Zhu, *J. Phys. Chem. C*, 2009, **113**, 19633–19638.

51 G. Huang, S. Zhang, T. Xu and Y. Zhu, *Environ. Sci. Technol.*, 2008, **42**, 8516–8521.

52 S. T. Chang, I. C. Leu and M. H. Hon, *J. Cryst. Growth*, 2004, **273**, 195–202.

53 J. Zhang, X. Liu, S. Wu, M. Xu, X. Guo and S. Wang, *J. Mater. Chem.*, 2010, **20**, 6453–6459.

54 H. Ahn, H. Choi, K. Park, S. Kim and Y. Sung, *J. Phys. Chem. B*, 2004, **108**, 9815–9820.

55 J. Zuo, C. Xu, X. Liu and C. Wanga, *J. Appl. Phys.*, 1994, **75**, 1835–1836.

56 P. D. Batista, M. Mulato, C. F. O. Graeff, F. J. R. Fernandez and F. C. B. Marques, *J. Phys.*, 2006, **36**, 478–481.

57 H. V. Vlekkert, L. Bousse and N. D. Rooij, *J. Colloid Interface Sci.*, 1988, **122**, 336–345.

58 M. R. Houchin and L. J. Warren, *J. Colloid Interface Sci.*, 1984, **100**, 278–286.

59 M. R. Houchin, *Colloids Surf.*, 1985, **13**, 125–136.

60 F. Kara, G. C. Gurakan and F. D. Sanin, *Biotechnol. Bioeng.*, 2008, **100**, 231–239.